Increased compression in HDC-based ablator implosions using modified drive profile

R. Tommasini ⬤, D. T. Casey, D. Clark, A. Do ⬤, K. L. Baker, O. L. Landen ⬤, V. A. Smalyuk, C. Weber, B. Bachmann,
E. Hartouni, S. Kerr, C. Krauland, E. V. Marley, M. Millot ⬤, J. Milovich, R. C. Nora ⬤, A. E. Pak, D. Schlossberg,
B. Woodworth, T. M. Briggs, D. M. Holunga ⬤, A. Nikroo, and M. Stadermann ⬤

Lawrence Livermore National Laboratory, 7000 East Avenue, Livermore, California 94550, USA

Compression is an essential component of achieving high gain in inertial confinement fusion. However, increasing compression with crystalline ablator-based implosions had not succeeded up to now, attributed to increased hydrodynamic instability growth. We present experimental results demonstrating record high compression of stagnated fuel in indirectly driven implosions that use a high-density carbon ablator at the National Ignition Facility (NIF) [Spaeth *et al.,* Fusion Sci. Technol. **69**, 25 (2016)] by the use of a modified drive pulse (and capsule design). Specifically, the SQ-n design [Clark *et al.,* Phys. Plasmas **29**, 052710 (2022)] replaces the second and the third shock phase with a more gently ramped rise designed to reduce in-flight fuel adiabat and instability growth at both the ablation front and the ablator-DT fuel interface and hence promote increased compression. Comparing the results from a large set of experiments, we show that SQ-n achieves ≈15%–30% higher compression than prior designs, a finding that may chart a path toward increased compression and higher gain at the NIF [Abu-Shawareb *et al.,* Phys. Rev. Lett. **129**, 075001 (2022).].

Laboratory experiments at the National Ignition Facility (NIF) [1] have exceeded Lawson's requirement in inertial confinement fusion (ICF) implosions for the first time [2]. These implosions use the x rays, generated by illuminating the inside of a gold hohlraum with 192 laser beams, to drive the implosion by the pressure produced from the soft x-ray ablation of a spherical, thin, low-Z capsule, i.e., the ablator, encasing a cryogenic layer of deuterium-tritium (DT) fuel. At stagnation, the shell and fuel kinetic energy is transferred to the internal energy of a hot spot to ignite a thermonuclear runaway that propagates into the dense fuel layer before disassembly. Eventually, the yield produced is limited by pdV expansion [3] that reduces the burn rate and sets a maximum burn fraction, $f_b = \rho R/(\rho R + 6)$, where ρR is the compressed fuel areal density in g/cm^2 [4]. Increasing the burn-up fraction beyond current experiments [2] is a main goal of the ICF program at NIF. One lever on compression is set by the entropy, or adiabat, established by the timing and strength of successive shocks used to compress the fuel before final acceleration [4]. Residual drive asymmetries limit the minimum achievable volume and generate additional parasitic modes through which the kinetic energy of the implosion can dissipate before being converted into hot spot internal energy and fuel compression [5]. The implosion is unstable at several interfaces, and at different stages, which causes small imperfections to grow, damaging the integrality of the shell, and mixing material between interfaces. In fact, it has been

hypothesized that in-flight mixing of an x-ray heated higher-Z hotter ablator into the colder fuel [6,7] is raising the entropy or adiabat of the fuel, limiting compression levels and ultimately gain [8]. Mitigating any instability growth that can reduce compression is necessary to achieve high gain at the current scale.

In this Letter, we report on experiments, denoted SQ-n [9,10], that have recorded high compression of the fuel in implosions using crystalline high-density carbon (HDC) ablators [11,12] at the NIF, a finding that supports the hypothesis that compression in HDC implosion experiments is degraded by instability growth. The degree of compression is quantified by the areal density, $\rho \Delta R$, achieved by the imploding shell as inferred from the fraction of neutrons produced in the hot spot that is down-scattered by the surrounding cold fuel in an implosion with a cryo fuel layer. This metric, the down-scattered ratio (DSR) [13–15], is numerically defined as the ratio of scattered neutrons with energies between 10 and 12 MeV over nonscattered, with energies between 13 and 17 MeV. Specifically, SQ-n DSR values (at a design adiabat ≈3) show ≈15% and 30% improvement over those of the higher design adiabat Bigfoot (BF) [16,17] (at a design adiabat ≈4.0) and the lower design adiabat HDC [18,19] (at a design adiabat ≈2.5) implosions at comparable implosion velocity and ice thickness. Therefore, the experiments employing the SQ-n design suggest that we have simultaneously successfully mitigated high mode growth at the ablator-fuel interface [12,20] present in the three-shock HDC design while improving the in-flight adiabat over the BF design [9].

The BF design uses a three-shock pulse shape, shown in Fig. 1, where the first and second shocks merge at the ablator-fuel interface and meet the third shock at the inner fuel surface, setting the shell at an adiabat $\alpha \sim 4$ [16,17]. In the
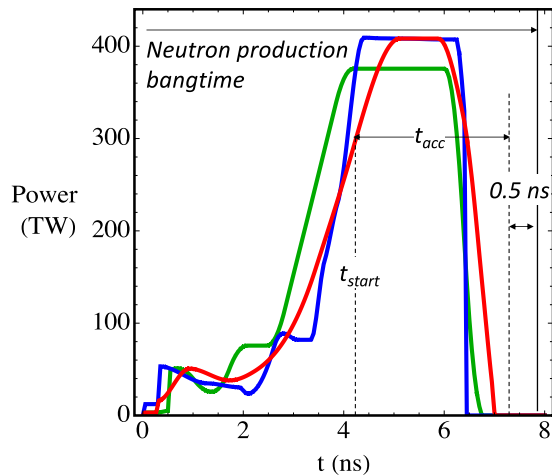
FIG. 1. Pulse shapes used in the experiments: SQ-n (red) vs HDC (blue) and BF (green). The vertical solid line indicates the neutron bangtime and it is used here to illustrate the definition of acceleration time, t_{acc}.

FIG. 2. Hohlraums and capsules used in the experiments. For the benefit of brevity, the two capsule varieties, (a) and (b), are referred to in the text as the "W-inner" and "W-buried" layer, respectively.

HDC design the pulse shape is timed to have the three shocks colliding at the inner fuel surface, for a resulting in-flight adiabat $\alpha \sim 2.5$ [18,19]. Early subscale experiments utilizing high-density carbon ablators with a "three-shock HDC" pulse shape yielded similar or lower measured DSR values than experiments with a "three-shock BF" pulse shape despite the former having a lower design adiabat. This result suggests an interface mix being responsible for compression degradation in the three-shock HDC design, and motivated the development of a pulse shape, "SQ-n," with improved stability to reduce the mix. As shown in Fig. 1, both the three-shock HDC and the SQ-n pulse shapes use a similar strength first shock that ensures melting of the HDC ablator to mitigate the seeding growth of instabilities in the initially crystalline material [11,12]. However, the similarities end here.

The passage of each shock in the HDC design leads to undesirable Richtmyer-Meshkov (RM) [21–33] growth of perturbations. When the shell starts to accelerate, the pressure and density gradients are subject to the violent Rayleigh-Taylor (RT) instability [34–38] at the ablation front such that perturbations established during the RM phase grow substantially larger at a nearly exponential rate. The ablation front density gradient and ablation velocity are stabilizing effects that suppress the growth of high modes during ablation. As the implosion begins to decelerate and approaches stagnation, perturbations will continue to grow due to the effects of spherical convergence, known as the Bell-Plesset effect [39–42]. Outer surface pits and bulk material voids can seed this instability growth and introduce high-Z material into the hot spot, increasing radiation losses and making material more difficult to compress, ultimately preventing ignition or limiting gain. Hydrodynamic instabilities at other interfaces in the capsule can mix material from the ablator into the DT raising entropy and reducing compression and limiting burn propagation after the hot spot is ignited. If the density of the ice fuel at the ice-ablator interface exceeds that of the HDC ablator, the sign of the Atwood number (At) is reversed making this interface classically stable to the RT instability during the acceleration phase of the implosion. The conditions at
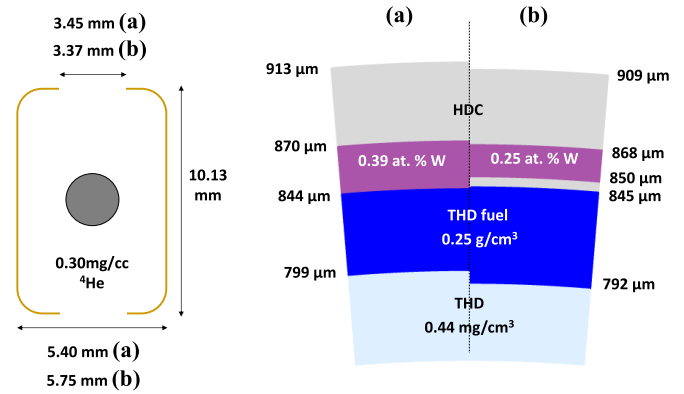
the ice-ablator interface depend on several factors, including the amount of hard spectrum x-ray preheat from the drive that can interact deep in the ablator. To help control the At, high-Z (typically W) dopant is added to the ablator. However, there are trade-offs in ablation efficiency and stability at the ablation front that must be considered and often allow positive At, at some point, that enables the growth of very small high-mode perturbations at the ice-ablator interface. This growth can introduce a hot ablator into the fuel making it more difficult to compress. In the three-shock HDC and BF designs, the dopant is buried inside the ablator, at $\approx 5\,\mu$m from the fuel outer surface [Fig. 2(b)], creating another interface of clean/doped material near the inner surface that can seed RM and RT growth. To fundamentally change these typical stability trade-offs, the SQ-n design uses a novel strategy to replace the second shock with a gently rising ramp setting the fuel at a low adiabat of 3, while accelerating the first shock as it goes through the ablator. This acceleration causes the perturbations in the RM phase to oscillate instead of growing linearly [21–33], effectively damping the shock-driven RM growth and greatly reducing the RT seeds at the ablator-fuel interface [9,10] and the final shock strength. Therefore, the fuel-ablator interface experiences only a single shock followed by a smooth, quasicontinuous acceleration. This can be seen in Fig. 3(a), showing the simulated velocity profiles,
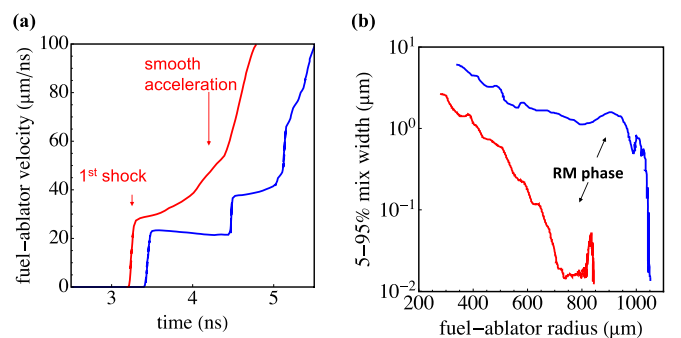

FIG. 3. Simulated velocity of the fuel-ablator interface shortly after the first shock crosses that interface (a) and mix width vs fuel ablator radius (b) for the three-shock HDC (blue) and SQ-n (red) designs. The comparisons show the improved stability and reduced mix achievable with the SQ-n design.

from the radiation hydrodynamics code HYDRA [43], of the fuel-ablator interface shortly after the first shock crosses that interface. This interface acceleration has the effect of turning this RM-unstable phase of the implosion into a RT-stable phase [9,10]. As a result, the mix width at the ablator-fuel interface is reduced by more than an order of magnitude at the end of the RM phase, for the SQ-n drive. Likewise, SQ-n design uses a dopant distribution where the doped ablator region extends all of the way to the fuel-ablator interface [Fig. 2(a)]. Since this brings the tungsten dopant (W) down to the HDC shell's inner edge, this dopant distribution is referred to as a W-inner dopant distribution. This replaces the typical buried layer dopant distribution that includes a thin undoped ablator layer between the DT fuel and the doped ablator region. The W-inner configuration removes one potentially unstable interface from the design, and preshot simulations suggested it can substantially reduce fuel-ablator mixing in SQ-n. Ultimately, Fig. 3(b) shows the simulated mix width vs fuel-ablator radius, revealing substantial mixing between the HDC and DT at the interface for the HyE implosion (black curve).

In the case of SQ-n and some HDC implosions, the 192 NIF beams drive a 5.4-mm-diameter cylindrical hohlraum containing a suspended capsule of inside radius 844 μm with a 69-μm-thick HDC ablator enclosing a 40–45-μm-thick cryogenic hydrogen isotope fuel layer. The ablator contains a 26-μm-thick, 0.39% W-doped layer, starting at 870 μm radius and extending all of the way to the inner edge of the ablator shell. This dopant layer configuration will be referred to as W-inner throughout this Letter. For the remaining HDC implosions, the hohlraum had a 5.75 mm diameter and the capsule an inside radius of 845 μm with a 64-μm-thick high-density carbon ablator, containing an 18-μm-thick, 0.25% W-doped layer, starting at 5 μm from the inner radius enclosing a 53-μm-thick cryogenic hydrogen isotope fuel layer [Fig. 2(b)]. This dopant layer configuration will be referred to as W-buried throughout this Letter.

The majority of the experiments discussed here used a cryogenic layer with a surrogate tritium-hydrogen mix in a ratio of 3:1, and a nominal deuterium fraction of 0.8%, maintaining hydro-equivalence to the usual 50/50 DT layers [44]. The NIF drive pulse delivered a total energy of 1.3–1.5 MJ, depending on the pulse duration, at 3ω (0.35 μm) with a peak power of 400 TW.

The x-ray core shape is measured by 40–90-ps gated >7 keV, 12–15× magnification, 10-μm pinhole imagers looking from both equatorial and polar lines of sight. This information was used to confirm that the cores did not have large mode 2–4 asymmetries that would bias the comparisons of compression achieved. Figure 4 shows the hot spot x-ray emission from two of the SQ-n experiments, N220501 and N220604, with overlays of the level contours at the 17% of peak emission. These contours are used to assess the hot spot size and asymmetry modes through a Legendre decomposition and shows the mode 2–4 asymmetries all below a level of 6% of the average radius.

An array of neutron energy sensitive detectors is used to measure the value of the DSR along five different lines of sight [45]. The measurements are fitted to a spherical harmonic expansion Y_{lm}, up to $l = 1$, to produce a DSR "skymap" and
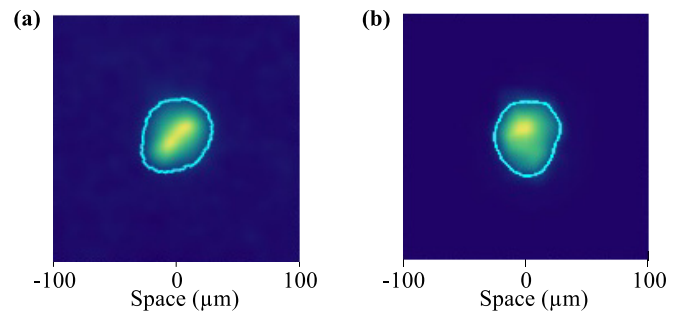

FIG. 4. Time-resolved x-ray emission images from SQ-n experiments N220501 (a) and N220604 (b), from equatorial lines of sight, with overlays of the 17%-of-peak-emission level contours. The resulting values for Legendre mode 2 and mode 4, expressed as a percentage of the average radius, are 3% and −4%, and 6% and −1%, for N220501 and N220604, respectively.

calculate the DSR average (over 4π) and any mode-1 DSR asymmetry [46]. Figure 5 shows the DSR skymaps for the four experiments that are part of the SQn series, together with the average and the minimum and maximum values of the DSR for each experiment. For a comparison across different designs, it is crucial to compensate the reduction in compression due to the induced asymmetries. An estimate of mode-1 asymmetry can be easily calculated from $\delta \text{DSR}/\text{DSR} = (\text{DSR}_{\max} - \text{DSR}_{\min})/(2\text{DSR}_{4\pi})$ and the values reported in Fig. 5. The experiment affected by the largest degree of asymmetry is N220115, for which $\delta \text{DSR}/\text{DSR} = 37\%$, with the other experiments ranging between 10% and 20%.

Therefore the DSR measured values are corrected for such mode-1 asymmetry reducing compression according to the factor $[1 - (\delta \text{DSR}/\text{DSR})^2]^{-1}$, validated by simulations and a piston model [47,48] and using amplitude values for mode 1 measured by nToF [49], RTNADs [50], and FNADs [51] detectors. While this correction, $\approx +4\%$ on average, may only be slightly larger than the raw data statistical error bars, it is important in ensuring a fair comparison.

To compare the fuel convergence ratios (a metric of compression), scaling as $\sqrt{(\rho \Delta R_{\text{final}}/\rho \Delta R_{\text{initial}})}$, the DSR values are also normalized to a nominal 45-μm initial thickness. The resulting values of DSR are shown in Fig. 6. It is evident from the plot that the SQ-n experiments have resulted in a significant increase in compression when compared to HDC and BF, as demonstrated by the higher, by far, recorded values of DSR.

Figure 6 shows the DSR values plotted against the implosion velocity v_{imp}. The values of the implosion velocity are derived from measured quantities according to $v_{\text{imp}} \sim R/t_{\text{acc}}$, where R is the capsule radius and the acceleration time t_{acc} is defined as $t_{\text{acc}} = t_{\text{BT}} - t_{\text{start}} - 0.5$ ns, where t_{BT} is the bang-time, and t_{start} is the time at which the drive power rises above 300 TW, being the final shock trajectory is not sensitive to peak powers above this threshold. This derivation of the implosion velocity has been validated against companion experiments that have measured the trajectory of the shell using in-flight radiography [52,53]. The values of the implosion velocity obtained this way are then normalized by the value directly measured on said radiography companion shots [8].

N220115: DSR (%) = 3.75 ± 0.15 | {min, max} = {2.3, 5.01}

N220320: DSR (%) = 3.33 ± 0.15 | {min, max} = {2.68, 3.82}

N220501: DSR (%) = 3.86 ± 0.14 | {min, max} = {3.4, 4.13}

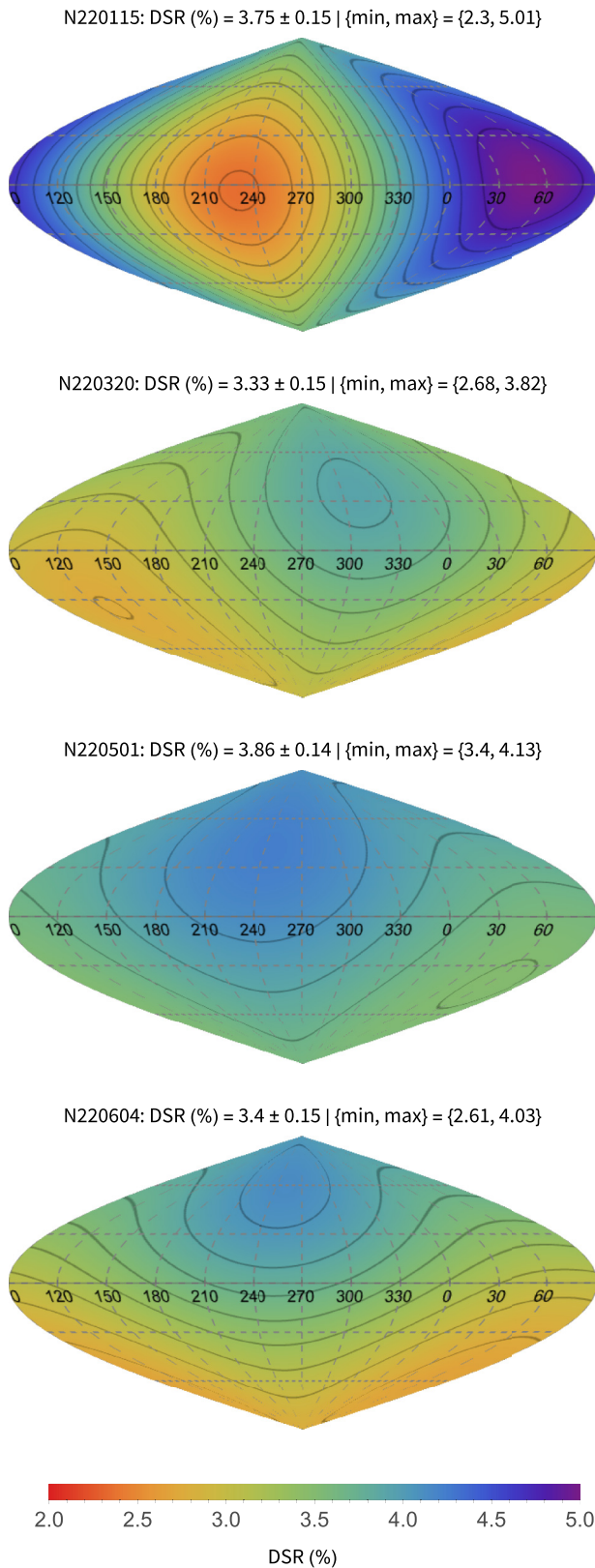N220604: DSR (%) = 3.4 ± 0.15 | {min, max} = {2.61, 4.03}

DSR (%)

FIG. 5. DSR skymaps for the four SQ-n experiments. The average and the minimum and maximum values of the DSR are reported on the header of the skymap of each experiment.
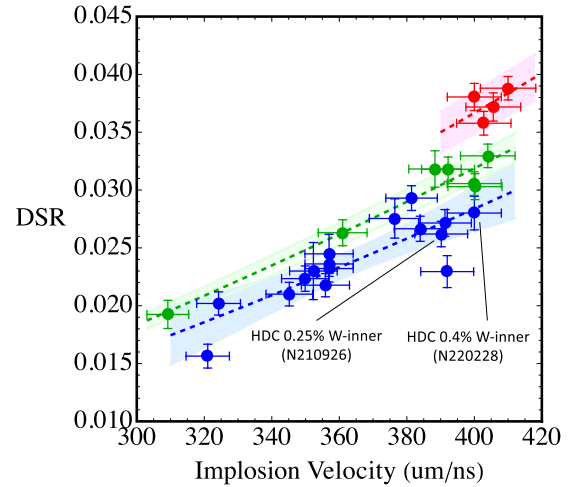
FIG. 6. BF (green), HDC (blue), and SQ-n (red) show the respective measured values of DSR parametrized vs implosion velocity. The down-scattered ratio values are corrected for mode-1 asymmetry and normalized to the 45-μm fuel ice layer. The fits, using Eq. (A5), include shaded areas representing the 95% confidence levels, i.e., 2σ.

This parametrization helps in separating statistically the different values of DSR for the three different designs and shows the trend of increasing DSR with increasing v_{imp}, in agreement with the scaling, Eq. (A5), derived in the Appendix, $DSR/M_{fuel} \sim v_{imp}^{1.6}/(f\alpha_{hs})$, with α_{hs} being the hot spot adiabat, and f a factor that accounts for any ablator-fuel mix preheating the fuel and reducing the stagnated fuel density and compression. To quantify the effective variations in DSR across the three designs, Fig. 6 shows the fits of the measured values of DSR to Eq. (A5), including shaded areas, representing the 95% confidence levels. The fact that these areas are not overlapping shows strong statistical independence between the results from the SQ-n and the non-SQ-n designs. From the fitted value of the multiplicative constant, we conclude that the DSR gains achieved by the SQ-n pulse are 15% ± 3% with respect to BF and 30% ± 4% with respect to HDC. Given that this constant corresponds to the factor $1/(f\alpha_{hs})$, we can ascribe the increased compression mainly to the reduced fuel ablator mix relative to the lower adiabat HDC design, and the lower adiabat relative to the BF design. The reduction of mix has been validated by using spectroscopy of the *L*-shell emission from W, along the polar line of sight [54–56]. Results show the SQ-n design to have greatly reduced mix signatures from both fuel-ablator and fuel–hot spot interfaces, as compared to three-shock HDC.

The W-inner dopant profile has also been tested in the three-shock HDC design but did not perform as well in terms of compression as SQ-n as shown in Fig. 6. This suggests that the ramped pulse shape is essential for the higher compression seen in SQ-n. The DSR does show a modest increase when the W-inner dopant layer concentration was increased from 0.25% (N210926) to 0.4% (N220228), but can be just ascribed, within error bars, to v_{imp} scaling.

In summary, we have presented experimental results demonstrating record high compression of stagnated fuel in implosions using the HDC ablator at the NIF. We notice that the highest DSR SQ-n shot matches, within error bars,

the fuel compression ratio achieved by the highest CH-based four-shock low adiabat design [57]. Further experiments are planned to optimize the dopant profile and content for the SQ-n design and to measure the stagnated peak fuel density and interface mix, to further understand the improvement in areal density using Compton radiography [5] and in-flight monochromatic radiography [58].

While ignition has been achieved in ICF experiments at the NIF [2], achieving even higher gains and efficient burn requires an increase in compression of the assembled fuel in large-scale implosions. The results presented here pave the way to 25% larger scale SQ-n experiments testing if higher compression can indeed increase fusion gain and surpass the recent breakthrough results reported by Abu-Shawareb *et al.* in Ref. [2]. As such, the presented work represents a transformative step forward in what we can strive to achieve in ICF.

Appendix. It is instructive to isolate the DSR dependence on parameters, such as peak velocity, adiabat, and mix, adding to a prior derivation [59], to compare to the existing data in Fig. 6. In what follows, we will assume that, in the deceleration phase, PV^γ is an approximate invariant of the hot spot during deceleration, and the stagnated fuel and hot spot are isobaric [60]. This has been shown by Saillard [61], using a zero-dimensional model of the implosion and one-dimensional (1D) simulations [cf. Eq. (4.33) and Fig. 10 of Ref. [61]], and by Bose *et al.* [62], using a one-dimensional model of the implosion [cf. Eqs. (17) and (18) in Ref. [62]].

We start by relating the isobaric stagnation energy to the peak fuel kinetic energy:

$$P_{\text{stag}} R_{\text{stag}}^3 \sim \eta M_{\text{fuel}} v_{\text{imp}}^2 \sim M_{\text{fuel}} v_{\text{imp}}^{1.6}, \quad (A1)$$

where P_{stag} and R_{stag} are the pressure and outer radius of the fuel at stagnation, M_{fuel} is the mass of the fuel, and v_{imp} is the fuel implosion velocity. The term η scales as $v_{\text{imp}}^{-0.4}$, and accounts for the loss of ablator remaining mass, per Rocket model and for fixed M_{fuel}, as v_{imp} increases, that results in decreasing push from the ablator and, ultimately, less compression than expected from an $\sim v_{\text{imp}}^2$ scaling [57,63].

Incorporating the definition of "adiabat," α, as per Eq. (1) in Ref. [28], into the ideal-gas adiabatic equation, we can then write $PV^\gamma \sim \alpha_{hs} M_{hs}^\gamma \sim c$, where α_{hs} and M_{hs} are the hot spot adiabat and mass. We now assume M_{hs} negligibly small with respect to M_{fuel} and constant across the different experiments as the initial radius and fill are similar between designs and the yield amplification is negligible. Substituting the value for a monatomic gas, $\gamma = 5/3$, we get (cf. Ref. [48])

$$P_{\text{stag}} R_{hs}^5 \sim c, \quad (A2)$$

where R_{hs} is the final radius of the hot spot. Furthermore, consistent with 1D simulations [63], we can approximate

$$R_{\text{stag}} \sim R_{hs} (f M_{\text{fuel}} / R^3)^{1/5} \quad (A3)$$

with R being the initial radius. This accounts for fuel thickness $\Delta R = R_{\text{stag}} - R_{hs}$ increasing with M_{fuel} at a given compressed fuel density ρ, and any ablator-fuel mix puffing up the fuel by a factor $f \sim \rho(\text{no mix})/\rho(\text{mix}) \sim [\alpha_{\text{fuel}}(\text{mix})/\alpha_{\text{fuel}}(\text{no mix})]^{3/5}$. Substituting for R_{hs} and for P_{stag} from Eq. (A1) in the limit of fixed initial radius we get

$$R_{\text{stag}}^2 \sim f c / v_{\text{imp}}^{1.6}. \quad (A4)$$

It should be noted that Eq. (A4) still holds if one more correctly replaces M_{fuel} with $M_{\text{fuel}} + M_{mix}$, where M_{mix} is the ablator mass mixed in the fuel by peak implosion velocity through to stagnation. Substituting for R_{stag} by invoking conservation of fuel mass given by, in valid approximation $\Delta R \ll R_{\text{stag}}$, $M_{\text{fuel}} \sim \rho R_{\text{stag}}^2 \Delta R$ we get

$$\frac{\rho \Delta R}{M_{\text{fuel}}} \sim \frac{\text{DSR}}{M_{\text{fuel}}} \sim \frac{v_{\text{imp}}^{1.6}}{f c} \quad (A5)$$

in the valid assumption that DSR is dominated by scattering off tritium-hydrogen-deuterium (THD) fuel and negligibly by doped HDC ablator, regardless of the level of mix.

[1] M. L. Spaeth, K. R. Manes, D. H. Kalantar, P. E. Miller, J. E. Heebner, E. S. Bliss, D. R. Spec, T. G. Parham, P. K. Whitman, and P. J. Wegner, Description of the NIF laser, Fusion Sci. Technol. **69**, 25 (2016).

[2] H. Abu-Shawareb *et al.* (Indirect Drive ICF Collaboration), Lawson criterion for ignition exceeded in an inertial fusion experiment, Phys. Rev. Lett. **129**, 075001 (2022).

[3] O. A. Hurricane, D. A. Callahan, D. T. Casey, E. L. Dewald, T. R. Dittrich, T. Döppner, S. Haan, D. E. Hinkel, L. F. Berzak Hopkins, O. Jones, A. L. Kritcher, S. Le Pape, T. Ma, A. G. MacPhee, J. L. Milovich, J. Moody, A. Pak, H.-S. Park, P. K. Patel, J. E. Ralph *et al.*, Inertially confined fusion plasmas dominated by alpha-particle self-heating, Nat. Phys. **12**, 800 (2016).

[4] J. Lindl, Development of the indirect-drive approach to inertial confinement fusion and the target physics basis for ignition and gain, Phys. Plasmas **2**, 3933 (1995).

[5] R. Tommasini, O. L. Landen, L. Berzak Hopkins, S. P. Hatchett, D. H. Kalantar, W. W. Hsing, D. A. Alessi, S. L. Ayers, S. D. Bhandarkar, M. W. Bowers, D. K. Bradley, A. D. Conder, J. M. Di Nicola, P. Di Nicola, L. Divol, D. Fittinghoff, G. Gururangan, G. N. Hall, M. Hamamoto, D. R. Hargrove *et al.*, Time-resolved fuel density profiles of the stagnation phase of indirect-drive inertial confinement implosions. Phys. Rev. Lett. **125**, 155003 (2020).

[6] B. A. Hammel, S. W. Haan, D. S. Clark, M. J. Edwards, S. H. Langer, M. M. Marinak, M. V. Patel, J. D. Salmonson, and H. A. Scott, High-mode Rayleigh-Taylor growth in NIF ignition capsules, High Energy Density Phys. **6**, 171 (2010).

[7] D. S. Clark, S. W. Haan, A. W. Cook, M. J. Edwards, B. A. Hammel, J. M. Koning, and M. M. Marinak, Short-wavelength and three-dimensional instability evolution in national ignition facility ignition capsule designs, Phys. Plasmas **18**, 082701 (2011).

[8] O. L. Landen, D. T. Casey, J. M. DiNicola, T. Doeppner, E. P. Hartouni, D. E. Hinkel, L. F. Berzak Hopkins, M. Hohenberger, A. L. Kritcher, S. LePape, B. J. MacGowan, S. Maclaren, K. D. Meaney, M. Millot, P. K. Patel, J. Park, L. A. Pickworth, H. F. Robey, J. S. Ross, S. T. Yang *et al.*, Yield and compression trends and reproducibility at NIF, High Energy Density Phys. **36**, 100755 (2020).

[9] D. S. Clark, D. T. Casey, C. R. Weber, O. S. Jones, K. L. Baker, E. L. Dewald, L. Divol, A. Do, A. L. Kritcher, O. L. Landen, and R. Tommasini, Exploring implosion designs for increased compression on the national ignition facility using high density carbon ablators, Phys. Plasmas **29**, 052710 (2022).

[10] C. R. Weber, D. S. Clark, D. T. Casey, G. N. Hall, O. Jones, O. Landen, A. Pak, and V. A. Smalyuk, Reduced mixing in inertial confinement fusion with early-time interface acceleration, Phys. Rev. E **108**, L023202 (2023).

[11] A. J. MacKinnon, N. B. Meezan, J. S. Ross, S. Le Pape, L. Berzak Hopkins, L. Divol, D. Ho, J. Milovich, A. Pak, J. Ralph, T. Döppner, P. K. Patel, C. Thomas, R. Tommasini, S. Haan, A. G. MacPhee, J. McNaney, J. Caggiano, R. Hatarik, R. Bionta *et al.*, High-density carbon ablator experiments on the National Ignition Facility, Phys. Plasmas **21**, 056318 (2014).

[12] S. J. Ali, P. M. Celliers, S. Haan, T. R. Boehly, N. Whiting, S. H. Baxamusa, H. Reynolds, M. A. Johnson, J. D. Hughes, and B. Watson, Probing the seeding of hydrodynamic instabilities from nonuniformities in ablator materials using 2D velocimetry, Phys. Plasmas **25**, 092708 (2018).

[13] V. Yu. Glebov, D. D. Meyerhofer, T. C. Sangster, C. Stoeckl, S. Roberts, C. A. Barrera, J. R. Celeste, C. J. Cerjan, L. S. Dauffy, D. C. Eder, R. L. Griffith, S. W. Haan, B. A. Hammel, S. P. Hatchett, N. Izumi, J. R. Kimbrough, J. A. Koch, O. L. Landen, R. A. Lerche, B. J. MacGowan *et al.*, Development of nuclear diagnostics for the National Ignition Facility (invited), Rev. Sci. Instrum. **77**, 10E715 (2006).

[14] J. A. Frenje, R. Bionta, E. J. Bond, J. A. Caggiano, D. T. Casey, C. Cerjan, J. Edwards, M. Eckart, D. N. Fittinghoff, S. Friedrich, V. Yu. Glebov, S. Glenzer, G. Grim, S. Haan, R. Hatarik, S. Hatchett, M. G. Johnson, O. S. Jones, J. D. Kilkenny, J. P. Knauer *et al.*, Diagnosing implosion performance at the Na-

[15] A. S. Moore, E. P. Hartouni, D. Schlossberg, S. Kerr, M. Eckart, J. Carrera, L. Ma, C. Waltz, D. Barker, and J. Gjemso, The five line-of-sight neutron time-of-flight (nToF) suite on the National Ignition Facility (NIF), Rev. Sci. Instrum. **92**, 023516 (2021).

[16] K. L. Baker, C. A. Thomas, D. T. Casey, S. Khan, B. K. Spears, R. Nora, T. Woods, J. L. Milovich, R. L. Berger, D. Strozzi, D. Clark, M. Hohenberger, O. A. Hurricane, D. A. Callahan, O. L. Landen, B. Bachmann, R. Benedetti, R. Bionta, P. M. Celliers, D. Fittinghoff *et al.*, High-performance indirect-drive cryogenic implosions at high adiabat on the National Ignition Facility, Phys. Rev. Lett. **121**, 135001 (2018).

[17] D. T. Casey, C. A. Thomas, K. L. Baker, B. K. Spears, M. Hohenberger, S. F. Khan, R. C. Nora, C. R. Weber, D. T. Woods, and O. A. Hurricane, The high velocity, high adiabat,"bigfoot" campaign and tests of indirect-drive implosion scaling, Phys. Plasmas **25**, 056308 (2018).

[18] L. Divol, A. Pak, L. F. Berzak Hopkins, S. Le Pape, N. B. Meezan, E. L. Dewald, D. D.-M. Ho, S. F. Khan, A. J. Mackinnon, J. S. Ross, D. P. Turnbull, C. Weber, P. M. Celliers, M. Millot, L. R. Benedetti, J. E. Field, N. Izumi, G. A. Kyrala, T. Ma, S. R. Nagel *et al.*, Symmetry control of an indirectly driven high-density-carbon implosion at high convergence and high velocity, Phys. Plasmas **24**, 056309 (2017).

[19] L. Berzak Hopkins, L. Divol, C. Weber, S. Le Pape, N. B. Meezan, J. S. Ross, R. Tommasini, S. Khan, D. D. Ho, J. Biener, E. Dewald, C. Goyon, C. Kong, A. Nikroo, A. Pak, N. Rice, M. Stadermann, C. Wild, D. Callahan, and O. Hurricane, Increasing stagnation pressure and thermonuclear performance of inertial confinement fusion capsules by the introduction of a high-Z dopant, Phys. Plasmas **25**, 080706 (2018).

[20] S. Davidovits, C. R. Weber, and D. S. Clark, Modeling ablator grain structure impacts in ICF implosions, Phys. Plasmas **29**, 112708 (2022).

[21] S. E. Bodner, D. G. Colombant, J. H. Gardner, R. H. Lehmberg, S. P. Obenschain, L. Phillips, A. J. Schmitt, J. D. Sethian, R. L. McCrory, W. Seka, C. P. Verdon, J. P. Knauer, B. B. Afeyan, and H. T. Powell, Direct-drive laser fusion: Status and prospects, Phys. Plasmas **5**, 1901 (1998).

[22] V. N. Goncharov, Theory of the ablative Richtmyer-Meshkov instability, Phys. Rev. Lett. **82**, 2091 (1999).

[23] N. Metzler, A. L. Velikovich, and J. H. Gardner, Reduction of early-time perturbation growth in ablatively driven laser targets using tailored density profiles, Phys. Plasmas **6**, 3283 (1999).

[24] Y. Aglitskiy, A. L. Velikovich, M. Karasik, V. Serlin, C. J. Pawley, A. J. Schmitt, S. P. Obenschain, A. N. Mostovych, J. H. Gardner, and N. Metzler, Direct observation of mass oscillations due to ablative Richtmyer-Meshkov instability in plastic targets, Phys. Rev. Lett. **87**, 265001 (2001).

[25] V. N. Goncharov, Analytical model of nonlinear, single-mode, classical Rayleigh-Taylor instability at arbitrary Atwood numbers, Phys. Rev. Lett. **88**, 134502 (2002).

[26] V. N. Goncharov, J. P. Knauer, P. W. McKenty, P. B. Radha, T. C. Sangster, S. Skupsky, R. Betti, R. L. McCrory, and D. D. Meyerhofer, Improved performance of direct-drive inertial confinement fusion target designs with adiabat shaping using an intensity picket, Phys. Plasmas **10**, 1906 (2003).

[27] K. Anderson and R. Betti, Theory of laser-induced adiabat shaping in inertial fusion implosions: The decaying shock, Phys. Plasmas **10**, 4448 (2003).

[28] R. Betti, K. Anderson, J. Knauer, T. J. B. Collins, R. L. McCrory, P. W. McKenty, and S. Skupsky, Theory of laser-induced adiabat shaping in inertial fusion implosions: The relaxation method, Phys. Plasmas **12**, 042703 (2005).

[29] O. V. Gotchev, V. N. Goncharov, J. P. Knauer, T. R. Boehly, T. J. B. Collins, R. Epstein, P. A. Jaanimagi, and D. D. Meyerhofer, Test of thermal transport models through dynamic overpressure stabilization of ablation-front perturbation growth in laser-driven CH foils, Phys. Rev. Lett. **96**, 115005 (2006).

[30] V. N. Goncharov, O. V. Gotchev, E. Vianello, T. R. Boehly, J. P. Knauer, P. W. McKenty, P. B. Radha, S. P. Regan, T. C. Sangster, S. Skupsky, V. A. Smalyuk, R. Betti, R. L. McCrory, D. D. Meyerhofer, and C. Cherfils-Clérouin, Early stage of implosion in inertial confinement fusion: Shock timing and perturbation evolution, Phys. Plasmas **13**, 012702 (2006).

[31] F. W. Doss, J. L. Kline, K. A. Flippo, T. S. Perry, B. G. DeVolder, I. Tregillis, E. N. Loomis, E. C. Merritt, T. J. Murphy, L. Welser-Sherrill, and J. R. Fincke, The shock/shear platform for planar radiation-hydrodynamics experiments on the National Ignition Facility, Phys. Plasmas **22**, 056303 (2015).

[32] K. A. Flippo, F. W. Doss, E. C. Merritt, B. G. DeVolder, C. A. Di Stefano, P. A. Bradley, D. Capelli, T. Cardenas, T. R. Desjardins, F. Fierro, C. M. Huntington, J. L. Kline, L. Kot, S. Kurien, E. N. Loomis, S. A. MacLaren, T. J. Murphy, S. R. Nagel, T. S. Perry, R. B. Randolph *et al.*, Late-time mixing and turbulent behavior in high-energy-density shear experiments at high Atwood numbers, Phys. Plasmas **25**, 056315 (2018).

[33] A. Do, C. R. Weber, E. L. Dewald, D. T. Casey, D. S. Clark, S. F. Khan, O. L. Landen, A. G. MacPhee, and V. A. Smalyuk, Direct measurement of ice-ablator interface motion for instability mitigation in indirect drive ICF implosions, Phys. Rev. Lett. **129**, 215003 (2022).

[34] D. Colombant, W. Manheimer, and E. Ott, Three-dimensional, nonlinear evolution of the Rayleigh-Taylor instability of a thin layer, Phys. Rev. Lett. **53**, 446 (1984).

[35] W. Manheimer, D. Colombant, and E. Ott, Three-dimensional, nonlinear evolution of the Rayleigh–Taylor instability of a thin layer, Phys. Fluids **27**, 2164 (1984).

[36] H. Takabe, K. Mima, L. Montierth, and R. L. Morse, Self-consistent growth rate of the Rayleigh–Taylor instability in an ablatively accelerating plasma, Phys. Fluids **28**, 3676 (1985).

[37] S. E. Bodner, M. H. Emery, and J. H. Gardner, The Rayleigh-Taylor instability in direct-drive laser fusion, Plasma Phys. Controlled Fusion (1987).

[38] S. Atzeni, Implosion symmetry and burn efficiency in ICF, Laser Part. Beams **9**, 233 (1991).

[39] P. Amendt, J. D. Colvin, J. D. Ramshaw, H. F. Robey, and O. L. Landen, Modified Bell–Plesset effect with compressibility: Application to double-shell ignition target designs, Phys. Plasmas **10**, 820 (2003).

[40] R. Epstein, On the Bell–Plesset effects: The effects of uniform compression and geometrical convergence on the classical Rayleigh–Taylor instability, Phys. Plasmas **11**, 5114 (2004).

[41] A. L. Velikovich and P. F. Schmit, Bell-Plesset effects in Rayleigh-Taylor instability of finite-thickness spherical and cylindrical shells, Phys. Plasmas **22**, 122711 (2015).

[42] Z. Wang, K. Xue, and P. Han, Bell–Plesset effects on Rayleigh–Taylor instability at cylindrically divergent interfaces between viscous fluids, Phys. Fluids **33**, 034118 (2021).

[43] M. M. Marinak, G. D. Kerbel, N. A. Gentile, O. Jones, D. Munro, S. Pollaine, T. R. Dittrich, and S. W. Haan, Three-dimensional hydra simulations of National Ignition Facility targets, Phys. Plasmas **8**, 2275 (2001).

[44] M. J. Edwards, J. D. Lindl, B. K. Spears, S. V. Weber, L. J. Atherton, D. L. Bleuel, D. K. Bradley, D. A. Callahan, C. J. Cerjan, D. Clark, G. W. Collins, J. E. Fair, R. J. Fortner, S. H. Glenzer, S. W. Haan, B. A. Hammel, A. V. Hamza, S. P. Hatchett, N. Izumi, B. Jacoby *et al.*, The experimental plan for cryogenic layered target implosions on the National Ignition Facility—The inertial confinement approach to fusion, Phys. Plasmas **18**, 051003 (2011).

[45] R. Hatarik, D. B. Sayre, J. A. Caggiano, T. Phillips, M. J. Eckart, E. J. Bond, C. Cerjan, G. P. Grim, E. P. Hartouni, J. P. Knauer, J. M. Mcnaney, and D. H. Munro, Analysis of the neutron time-of-flight spectra from inertial confinement fusion experiments, J. Appl. Phys. **118**, 184502 (2015).

[46] E. P. Hartouni, R. M. Bionta, D. T. Casey, M. J. Eckart, M. Gatu-Johnson, G. P. Grim, K. D. Hahn, J. Jeet, S. M. Kerr, A. L. Kritcher, B. J. MacGowan, A. S. Moore, D. H. Munro, D. J. Schlossberg, and A. Zylstra, Interpolating individual line-of-sight neutron spectrometer measurements onto the "sky" at the National Ignition Facility (NIF), Rev. Sci. Instrum. **92**, 043512 (2021).

[47] O. A. Hurricane, D. T. Casey, O. Landen, A. L. Kritcher, R. Nora, P. K. Patel, J. A. Gaffney, K. D. Humbird, J. E. Field, M. K. G. Kruse, J. L. Peterson, and B. K. Spears, An analytic asymmetric-piston model for the impact of mode-1 shell asymmetry on ICF implosions, Phys. Plasmas **27**, 062704 (2020).

[48] O. A. Hurricane, D. T. Casey, O. Landen, D. A. Callahan, R. Bionta, S. Haan, A. L. Kritcher, R. Nora, P. K. Patel, and P. T. Springer, Extensions of a classical mechanics "piston-model" for understanding the impact of asymmetry on ICF implosions: The cases of mode 2, mode 2/1 coupling, time-dependent asymmetry, and the relationship to coast-time, Phys. Plasmas **29**, 012703 (2022).

[49] V. Yu. Glebov, III, T. C. Sangster, C. Stoeckl, J. P. Knauer, W. Theobald, K. L. Marshall, M. J. Shoup, T. Buczek, M. Cruz, T. Duffy, M. Romanofsky, M. Fox, A. Pruyne, M. J. Moran, R. A. Lerche, J. McNaney, J. D. Kilkenny, M. J. Eckart, D. Schneider, D. Munro *et al.*, The National Ignition Facility neutron time-of-flight system and its initial performance (invited). Rev. Sci. Instrum. **81**, 10D325 (2010).

[50] R. M. Bionta, G. P. Grim, K. D. Hahn, E. P. Hartouni, E. A. Henry, H. Y. Khater, A. S. Moore, and D. J. Schlossberg, Real-time nuclear activation detectors for measuring neutron angular distributions at the National Ignition Facility, Rev. Sci. Instrum. **92**, 043527 (2021).

[51] C. B. Yeamans and D. L. Bleuel, The spatially distributed neutron activation diagnostic FNADs at the National Ignition Facility, Fusion Sci. Technol. **72**, 120 (2017).

[52] D. G. Hicks, N. B. Meezan, E. L. Dewald, A. J. Mackinnon, R. E. Olson, D. A. Callahan, T. Döppner, L. R. Benedetti, D. K. Bradley, P. M. Celliers, D. S. Clark, P. Di Nicola, S. N. Dixit, E. G. Dzenitis, J. E. Eggert, D. R. Farley, J. A. Frenje, S. M. Glenn, S. H. Glenzer, A. V. Hamza *et al.*, Implosion dynamics

measurements at the National Ignition Facility, Phys. Plasmas **19**, 122702 (2012).

[53] J. R. Rygg, O. S. Jones, J. E. Field, M. A. Barrios, L. R. Benedetti, G. W. Collins, D. C. Eder, M. J. Edwards, J. L. Kline, J. J. Kroll, O. L. Landen, T. Ma, A. Pak, J. L. Peterson, K. Raman, R. P. J. Town, and D. K. Bradley, 2D x-ray radiography of imploding capsules at the National Ignition Facility, Phys. Rev. Lett. **112**, 195001 (2014).

[54] E. V. Marley, D. A. Liedahl, M. B. Schneider, R. F. Heeter, L. C. Jarrott, C. W. Mauche, G. E. Kemp, M. E. Foord, Y. Frank, and K. Widmann, Using L-shell x-ray spectra to determine conditions of non-local thermal dynamic equilibrium plasmas, Rev. Sci. Instrum. **89**, 10F106 (2018).

[55] C. R. Weber, D. S. Clark, A. Pak, N. Alfonso, B. Bachmann, L. F. Berzak Hopkins, T. Bunn, J. Crippen, L. Divol, and T. Dittrich, Mixing in ICF implosions on the National Ignition Facility caused by the fill-tube, Phys. Plasmas **27**, 032703 (2020).

[56] B. Bachmann, S. A. MacLaren, S. Bhandarkar, T. Briggs, D. Casey, L. Divol, T. Döppner, D. Fittinghoff, M. Freeman, S. Haan *et al.*, Measurement of dark ice-ablator mix in inertial confinement fusion, Phys. Rev. Lett. **129**, 275001 (2022).

[57] O. L. Landen, J. D. Lindl, S. W. Haan, D. T. Casey, P. M. Celliers, D. N. Fittinghoff, N. Gharibyan, V. N. Goncharov, G. P. Grim, E. P. Hartouni, O. A. Hurricane, B. J. MacGowan, S. A. MacLaren, K. D. Meaney, M. Millot, J. L. Milovich,

P. K. Patel, H. S. Robey, P. T. Springer, P. L. Volegov and M. J. Edwards, Fuel convergence sensitivity in indirect drive implosions, Phys. Plasmas **28**, 042705 (2021).

[58] G. N. Hall, C. M. Krauland, M. S. Schollmeier, G. E. Kemp, J. G. Buscho, R. Hibbard, N. Thompson, E. R. Casco, M. J. Ayers, and S. L. Ayers, The crystal backlighter imager: A spherically bent crystal imager for radiography on the National Ignition Facility, Rev. Sci. Instrum. **90**, 013702 (2019).

[59] C. A. Thomas, E. M. Campbell, K. L. Baker, D. T. Casey, M. Hohenberger, A. L. Kritcher, B. K. Spears, S. F. Khan, R. Nora, and D. T. Woods, Principal factors in performance of indirect-drive laser fusion experiments, Phys. Plasmas **27**, 112712 (2020).

[60] J. Meyer-ter Vehn, S. Atzeni, and R. Ramis, Inertial confinement fusion, Europhys. News **29**, 202 (1998).

[61] Y. Saillard, Acceleration and deceleration model of indirect drive ICF capsules, Nucl. Fusion **46**, 1017 (2006).

[62] A. Bose, R. Betti, D. Shvarts, and K. M. Woo, The physics of long- and intermediate-wavelength asymmetries of the hot spot: Compression hydrodynamics and energetics, Phys. Plasmas **24**, 102704 (2017).

[63] J. D. Lindl, S. W. Haan, O. L. Landen, A. R. Christopherson, and R. Betti, Progress toward a self-consistent set of 1D ignition capsule metrics in ICF, Phys. Plasmas **25**, 122704 (2018).